ARCHIVES OF ELECTRICAL ENGINEERING VOL. 75(1), pp. 177–190 (2026)

DOI 10.24425/aee.2026.156808

# High frequency simulation of multi-layer air core solenoids using FEM analysis

MOHAMMAD SEYDI [1], HASSAN REZA MIRZAEI [1]✉, EBRAHIM RAHIMPOUR [2]

[1] *Department of Electrical Engineering, Faculty of Engineering, University of Zanjan Iran*

[2] *Institute of Electrical Power Engineering and High Voltage Technology (IEHT) Technical University of Applied Sciences Würzburg-Schweinfurt Germany*

*e-mail: {m.seydi/✉ hr.mirzaei}@znu.ac.ir, ebrahim.rahimpour@thws.de*

(Received: 21.09.2025, revised: 29.01.2026)

**Abstract:** Air core solenoids are used widely as low-pass or band-pass filters in high voltage applications. To design a suitable solenoid with the desired Frequency Response (FR), a valid simulation model is required. The models typically used for this purpose are valid up to 1 MHz; however, in some cases, the behavior of such filters may be required in higher frequency ranges. This paper presents a detailed model for the multi-layer solenoid windings which is valid up to 5 MHz. To increase the model accuracy in the High Frequency (HF) ranges, the circuit elements of the model are calculated using the Finite Element Method (FEM). Additionally, the influence of the electromagnetic phenomena at high frequencies is investigated in FEM analysis. Moreover, in the case of multi-layer solenoids, the influence of the winding direction of different layers on the FR are investigated. To validate the simulation methodology, some solenoid windings are manufactured and subjected to Frequency Response Analysis (FRA) tests. Subsequently, the simulated and measured frequency responses of the windings are compared.

**Key words:** finite element method, frequency response analysis, high frequency simulation, solenoid windings

## 1. Introduction

Solenoid windings have no magnetic cores and, therefore, are usually called air-core windings. This type of winding is commonly used in low-pass or band-pass HV filters, such as the one used in partial discharge tests. To obtain the Frequency Response (FR) of such filters, various

models have been reported in recent researches. In [1] and [2], a single unit containing lumped RLC elements is used as a model of the solenoids, as shown in Fig. 1(a). This simplified model is valid at low frequencies and can correctly simulate just the first resonance frequency of the solenoids. To increase the accuracy of the model at High Frequency (HF) ranges, detailed models are employed in [3–5] as shown in Fig. 1(b). In this model, each RLC unit represents one or several turns of the winding. Since numerous RLC units are used in detailed models, they can simulate the electromagnetic behavior of the windings at HF ranges with more accuracy. On the other hand, detailed models are more complex and require additional computation time and effort [5, 6].

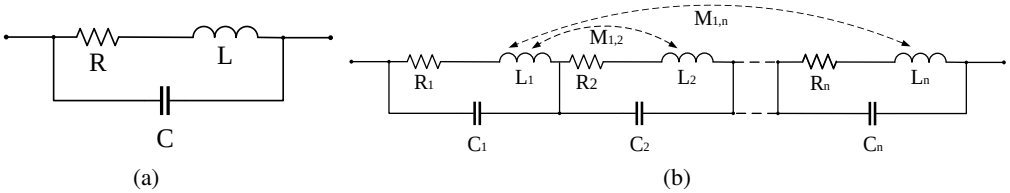


Fig. 1. The models of solenoid winding: simplified single unit RLC model (a); equivalent circuit of detailed model (b)

Accurate determination of the model elements' values is crucial. For this purpose, theoretical equations are proposed and utilized in [3–6]. However, the approximations that are used in such equations cause some deviations in the frequency response of the winding at HF ranges. To solve this problem, some researchers have utilized Finite Element Analysis (FEA) to accurately obtain the parameters of the model [7–11]. In [7, 8], and [11], numerical equations are employed to calculate the capacitance between the turns. Similarly, the resistances of the model are investigated in [12] based on the winding losses, which are influenced by the skin and proximity effects. Due to the nonlinear behavior of the current distribution in the wire cross-section at different frequencies, the resistances of the turns are frequency-dependent, and therefore, numerical FEA is commonly used to calculate their values [13–15]. Likewise, some theoretical and numerical equations for inductance calculation are proposed in [2], and [10]. For the sake of simplicity, a frequency-independent behavior is assumed for the inductance in these equations. However, frequency-dependent current distribution in the wire suggests that the inductance should be similarly frequency-dependent.

In this paper, the current distribution is investigated by FEA in more detail, and the resistance and inductance values are calculated with respect to the frequency. Additionally, the frequency response of multi-layer air core windings is investigated in the HF range, including 10 Hz to 5 MHz. Furthermore, the effect of winding direction of different layers is inspected by both simulation and measurement results. To verify the model's accuracy, two test windings are manufactured and their measured FRs are compared with the simulated ones.

The paper is organized as follows: Section 2 presents the detailed RLC model of the test windings. Then, in Section 3, the method for calculating RLC elements based on FEA is discussed. Section 4 presents the validation of the simulation model with experimental test results. Finally, Section 5 includes the discussion and conclusion.

## 2. The proposed models for the test windings

### 2.1. The test windings

To study the frequency response of the multi-layer solenoids, two test windings are designed and manufactured; both of them are made up of two concentric layers. The inner layers of both test windings are identical and wounded clockwise. Likewise, their outer layers are similar, except for the winding direction; the outer layer of the first test winding is counterclockwise, while the outer layer of the second one is clockwise. The diameters of the outer and inner layers are 250 mm and 200 mm, respectively. All layers consist of 100 turns of copper wire of 4 mm diameter coated with epoxy resin with a thickness of 0.04 mm.

### 2.2. The equivalent circuits

The equivalent circuits of the test windings are shown in Fig. 2, where each $n_t = 4$ turns are considered as one unit in the model, resulting in $n = 25$ units for each layer. In the models, $R_i$, $L_i$, and $C_{si}$ are the resistance, inductance, and the series capacitance of the $i$-th unit, respectively; the $M_{ij}$ is the mutual inductance between the $i$-th and $j$-th units, and $Cp_i$ is the parallel capacitance between the $i$-th unit in the outer layer and its opposite unit at the inner layer. Additionally, $R_E$ is the earth resistance that is connected to the end of the winding.

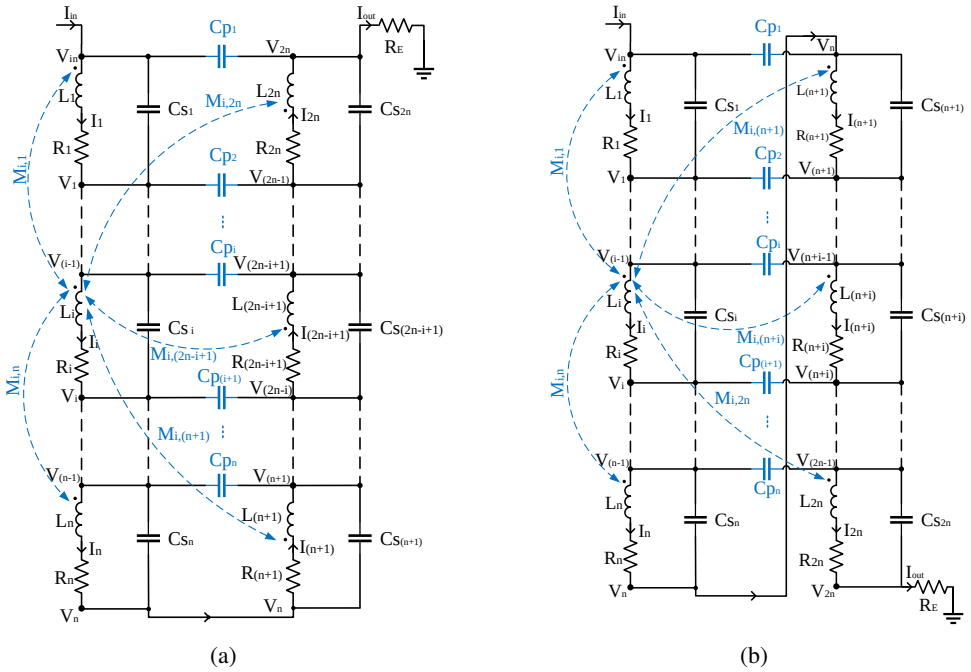


(a) (b)

Fig. 2. The detailed model of the first (a) and second (b) test windings

As is illustrated in Fig. 2, due to the winding directions of the layers, the last turns of the outer and inner layers of the first test winding are connected to each other, while in the case of the second test winding, the last turn of the outer layer is connected to the first turn of the inner layer.

### 2.3. The model equations

To achieve the relevant equations of the proposed model, Kirchhoff's circuit laws are employed. Using the KCL and KVL relationships, the equations could be obtained in matrix form. For the first test winding (Fig. 2(a)), the KCLs result in the following equations:

$$A_{2n\times 2n} \times I_{2n\times 1} - B_{1_{2n\times 1}} = Y_{2n?\times 2n} \times V_{2n\times 1}, \tag{1}$$

where:

$$A = \begin{bmatrix} 1 & -1 & 0 & \cdots & 0 & 0 & 0 \\ 0 & 1 & -1 & \cdots & 0 & 0 & 0 \\ 0 & 0 & 1 & \cdots & 0 & 0 & 0 \\ \vdots & \vdots & \vdots & \ddots & \vdots & \vdots & \vdots \\ 0 & 0 & 0 & \cdots & 1 & -1 & 0 \\ 0 & 0 & 0 & \cdots & 0 & 1 & -1 \\ 0 & 0 & 0 & \cdots & 0 & 0 & 1 \end{bmatrix}_{2n\times 2n},$$

$$I = \begin{bmatrix} I_1 \\ \vdots \\ I_i \\ \vdots \\ I_{(2n-i+1)} \\ \vdots \\ I_{2n} \end{bmatrix}_{2n\times 1}, \quad B_1 = \begin{bmatrix} C_{s1}V_{\text{in}} \\ 0 \\ 0 \\ \vdots \\ 0 \\ 0 \end{bmatrix}_{2n\times 1}, \quad V = \begin{bmatrix} V_1 \\ \vdots \\ V_i \\ \vdots \\ V_{(2n-i+1)} \\ \vdots \\ V_{2n} \end{bmatrix}_{2n\times 1},$$

also

$$Y = j\omega C_{1_{2n\times 2n}} - j\omega C_{2_{2n\times 2n}} + Y_{R_{2n\times 2n}}, \tag{2}$$

where:

$$\boldsymbol{C_1} = \begin{array}{c} \\ (1) \\ (2) \\ (3) \\ \\ (2n-1) \\ (2n) \end{array} \begin{array}{c} \begin{array}{ccccccc} (1) & (2) & (3) & \cdots & (2n-1) & (2n) \end{array} \\ \begin{bmatrix} C_{s1}+C_{p2}+C_{s2} & -C_{s2} & 0 & \cdots & 0 & 0 \\ -C_{s2} & C_{s2}+C_{p3}+C_{s3} & -C_{s3} & \cdots & 0 & 0 \\ 0 & -C_{s3} & C_{s3}+C_{p4}+C_{s4} & \cdots & 0 & 0 \\ \vdots & \vdots & \vdots & \ddots & \vdots & \vdots \\ 0 & 0 & 0 & \cdots & C_{s(2n+1)}+C_{p2}+C_{s2n} & -C_{s2n} \\ 0 & 0 & 0 & \cdots & -C_{s2n} & C_{s2n}+C_{p1} \end{bmatrix}_{2n\times 2n} \end{array},$$

$$\boldsymbol{C_2} = \begin{array}{c} \\ (1) \\ (2) \\ \\ (n-1) \\ (n) \\ (n+1) \\ \\ (2n-2) \\ (2n-1) \\ (2n) \end{array} \begin{array}{c} \begin{array}{ccccccccccc} (1) & (2) & & (n-1) & (n) & (n+1) & & (2n-2) & (2n-1) & (2n) \end{array} \\ \begin{bmatrix} 0 & 0 & \cdots & 0 & 0 & 0 & \cdots & 0 & C_{p2} & 0 \\ 0 & 0 & \cdots & 0 & 0 & 0 & \cdots & C_{p3} & 0 & 0 \\ \vdots & \vdots & \ddots & \vdots & \vdots & \vdots & \ddots & \vdots & \vdots & \vdots \\ 0 & 0 & \cdots & 0 & 0 & C_{pn} & \cdots & 0 & 0 & 0 \\ 0 & 0 & \cdots & 0 & 0 & 0 & \cdots & 0 & 0 & 0 \\ 0 & 0 & \cdots & C_{pn} & 0 & 0 & \cdots & 0 & 0 & 0 \\ \vdots & \vdots & \ddots & \vdots & \vdots & \vdots & \ddots & \vdots & \vdots & \vdots \\ 0 & C_{p3} & \cdots & 0 & 0 & 0 & \cdots & 0 & 0 & 0 \\ C_{p2} & 0 & \cdots & 0 & 0 & 0 & \cdots & 0 & 0 & 0 \\ 0 & 0 & \cdots & 0 & 0 & 0 & \cdots & 0 & 0 & 0 \end{bmatrix}_{2n\times 2n} \end{array},$$

$$Y_R = \begin{bmatrix} 0 & 0 & 0 & \cdots & 0 \\ 0 & 0 & 0 & \cdots & 0 \\ 0 & 0 & 0 & \cdots & 0 \\ \vdots & \vdots & \vdots & \ddots & \vdots \\ 0 & 0 & 0 & \cdots & \dfrac{1}{R_E} \end{bmatrix}_{2n\times 2n}.$$

Similarly, the KVLs result in:

$$-A^T_{2n\times 2n} \times V_{2n\times 1} + B_{2_{2n\times 1}} = Z_{2n\times 2n} \times I_{2n\times 1}, \tag{3}$$

where:

$$B_2 = \begin{bmatrix} V_{\text{in}} \\ 0 \\ 0 \\ \vdots \\ 0 \\ 0 \end{bmatrix}_{2n\times 1},$$

$$Z = \begin{bmatrix} R_1 + j\omega M_{1,1} & j\omega M_{1,2} & j\omega M_{1,3} & \cdots & j\omega M_{1,2n} \\ j\omega M_{2,1} & R_2 + j\omega M_{2,2} & j\omega M_{2,3} & \cdots & j\omega M_{2,2n} \\ j\omega M_{3,1} & j\omega M_{3,2} & R_3 + j\omega M_{3,3} & \cdots & j\omega M_{3,3n} \\ \vdots & \vdots & \vdots & \ddots & \vdots \\ j\omega M_{2n,1} & j\omega M_{2n,2} & j\omega M_{2n,3} & \cdots & R_{2n} + j\omega M_{2n,2n} \end{bmatrix}_{2n\times 2n},$$

where $\omega = 2\pi f$ is the angular frequency. In the same way, similar equations can be obtained for the model of the second test winding (Fig. 2(b)), except that the matrices $\boldsymbol{C_1}$ and $\boldsymbol{C_2}$ must be replaced as follows:

$$\boldsymbol{C_1} = \begin{array}{c} \\ (1) \\ (2) \\ (3) \\ \\ (2n-1) \\ (2n) \end{array} \begin{array}{c} \begin{array}{ccccccc} (1) & (2) & (3) & \cdots & (2n-1) & (2n) \end{array} \\ \begin{bmatrix} C_{s1}+C_{p2}+C_{s2} & -C_{s2} & 0 & \cdots & 0 & 0 \\ -C_{s2} & C_{s2}+C_{p3}+C_{s3} & -C_{s3} & \cdots & 0 & 0 \\ 0 & -C_{s3} & C_{s3}+C_{p4}+C_{s4} & \cdots & 0 & 0 \\ \vdots & \vdots & \vdots & \ddots & \vdots & \vdots \\ 0 & 0 & 0 & \cdots & C_{s(2n+1)}+C_{pn}+C_{s2n} & 0 \\ 0 & 0 & 0 & \cdots & -C_{s2n} & C_{s2n} \end{bmatrix}_{2n\times 2n} \end{array},$$

$$
\boldsymbol{C_2} = \begin{array}{c} \\ (1) \\ (2) \\ \\ (n-1) \\ (n) \\ (n+1) \\ (n+2) \\ \\ (2n-1) \\ (2n) \end{array}
\begin{bmatrix}
(1) & (2) & & (n-1) & (n) & (n+1) & (n+2) & & (2n-2) & (2n) \\
0 & 0 & \cdots & 0 & 0 & C_{p2} & 0 & \cdots & 0 & 0 \\
0 & 0 & \cdots & 0 & 0 & 0 & C_{p3} & \cdots & 0 & 0 \\
\vdots & \vdots & \ddots & \vdots & \vdots & \vdots & \vdots & \ddots & \vdots & \vdots \\
0 & 0 & \cdots & 0 & 0 & 0 & 0 & \cdots & C_{pn} & 0 \\
0 & 0 & \cdots & 0 & 0 & 0 & 0 & \cdots & 0 & 0 \\
C_{p2} & 0 & \cdots & 0 & 0 & 0 & 0 & \cdots & 0 & 0 \\
0 & C_{p3} & \cdots & 0 & 0 & 0 & 0 & \cdots & 0 & 0 \\
\vdots & \vdots & \ddots & \vdots & \vdots & \vdots & \vdots & \ddots & \vdots & \vdots \\
0 & 0 & \cdots & C_{pn} & 0 & 0 & 0 & \cdots & 0 & 0 \\
0 & 0 & \cdots & 0 & 0 & 0 & 0 & \cdots & 0 & 0
\end{bmatrix}_{2n\times 2n}.
$$

### 2.4. The transfer function

The characteristic impedance ($Z$) of the test windings is considered as the transfer function (TF), which can be obtained as the ratio of the input voltage to the input current [16, 17]:

$$Z(\boldsymbol{f}) = \frac{V_{\text{in}}(\boldsymbol{f})}{I_{\text{in}}(\boldsymbol{f})}, \tag{4}$$

where $\boldsymbol{f}$ is a discrete frequency vector, consisting of 1601 logarithmically spaced frequency samples from 10 Hz to 5 MHz. To simulate and achieve the TF at any desired frequency, the winding end is solidly grounded, $R_E = 0\ \Omega$, and then, the (1) and (3) are solved to obtain $I_{\text{in}}$ with respect to $V_{\text{in}}$.

## 3. The RLC elements calculation methodology

In order to estimate the values of equivalent circuit elements, the FEA is implemented by using COMSOL Multiphysics software.

### 3.1. The capacitance calculation

To obtain the capacitance between two adjacent turns ($C_{tt}$), the geometry shown in Fig. 3(a) is simulated in COMSOL, and Electrostatic Physics is adopted. By applying a $\Delta V$ voltage difference between these two turns and finding the electrostatic energy ($W_e$), the equivalent capacitance can be calculated as:

$$C_{tt} = 2 \times \frac{W_e}{\Delta V^2}, \tag{5}$$

According to Fig. 3(b), the equivalent series capacitance of each unit will be $C_{tt}/(n_t - 1)$. The results of the simulations are represented in Table 1 and have been verified by comparing their values with the results obtained from the analytical equations suggested in [1, 6, 7].

Likewise, the parallel capacitance between two opposite units at two adjacent layers ($Cp_i$) can be calculated by finding the electrostatic energy (Fig. 4) using COMSOL.

Table 1. Comparing the results of $C_{tt}$ at inner and outer layers obtained by the FEA and some theoretical methods

| | **Method** | | | |
|---|---|---|---|---|
| | **FEM simulation** | [1] | [6] | [7] |
| **Inner layer** | 173 pF | 171 pF | 156 pF | 169 pF |
| **Outer layer** | 196 pF | 188 pF | 191 pF | 189 pF |

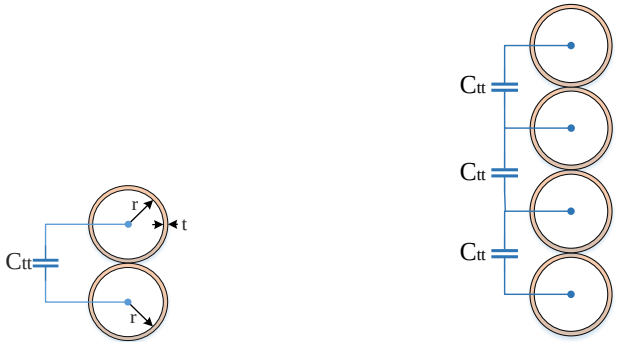


Fig. 3. The simulation geometry for calculating turn-to-turn capacitance (a), and the internal capacitances of one unit consisting of $n_t = 4$ turns (b)

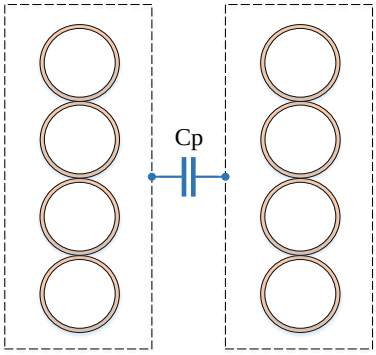


Fig. 4. The equivalent parallel capacitance of two opposite units

### 3.2. The inductance calculation

As was mentioned in the previous section, the value of the inductance depends on the frequency; therefore, its simulation is performed in the magnetic field physics of the COMSOL using a frequency-dependent study. Each unit is simulated by all its $n_t$ turns to calculate the

self-inductance based on the magnetic energy. Thus, the self-inductance of the unit is obtained as follows;

$$M_{ii} = 2 \times \frac{W_m}{I^2}, \tag{6}$$

where $W_m$ is the total stored energy in the simulation area, $M_{ii}$ is the equivalent inductance of the $i$-th unit, and $I$ is the electrical current flow through the turns. The self-inductance results obtained by the simulation are given in Table 2. To verify the simulation results, the obtained values have been compared with the results of some theoretical approaches. According to this table, the simulation results in the low frequency range (50 Hz) are in good agreement compared to the results of other references.

Table 2. The self-inductance results of the considered units

| | **Method** | | | |
|---|---|---|---|---|
| | **FEM simulation (at 50 Hz)** | [1] | [2] | [10] |
| **Inner layer** | 6.47 μH | 6.50 μH | 6.51 μH | 6.58 μH |
| **Outer layer** | 8.64 μH | 8.71 μH | 8.70 μH | 8.75 μH |

In addition, unlike the conventional methods in winding simulations, where constant values for the inductances are used, the inductance value decreases by about 6.2% when the frequency increases from 10 Hz to 5 MHz, as shown in Fig. 5.

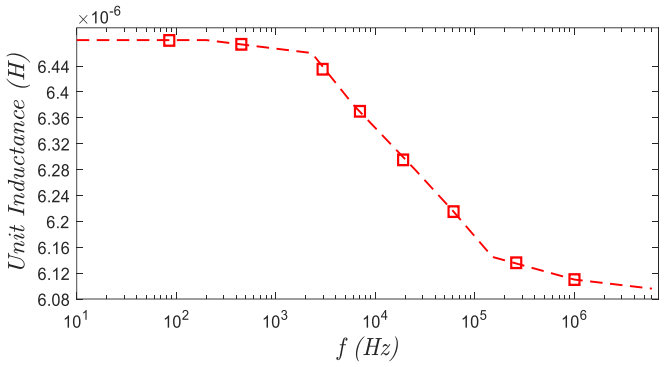


Fig. 5. The changes of a unit self-inductance in the studied frequency range

Likewise, the mutual inductance between two different units, whether they are in the same layer or not, can be calculated similarly by considering their turns in the simulation space. The mutual inductance between the $i$-th and $j$-th units could be found by obtaining the total magnetic energy in COMSOL:

$$M_{ij} = \frac{\left(2 \times \frac{W_m}{I^2} - M_{ii} - M_{jj}\right)}{2}. \tag{7}$$

### 3.3. The resistance calculation

Due to the nonlinear current distribution in the wire cross-section at HF, the resistance values strongly depend on the frequency. As the frequency increases, the uniform distribution of the current density across the wire is disturbed; the current tends to flow more through the lateral surfaces of the conductor. Therefore, the effective cross-sectional area decreases. In this case, the Skin and Proximity effects are two electromagnetic phenomena that affect the inhomogeneous HF current density [12–14]. In order to consider these effects simultaneously on the resistance value, similar to the inductance calculations, the magnetic field physics and frequency-dependent study of COMSOL are adopted. Accordingly, the magnetic field and current distribution on the surface of a unit are represented in Fig. 6.

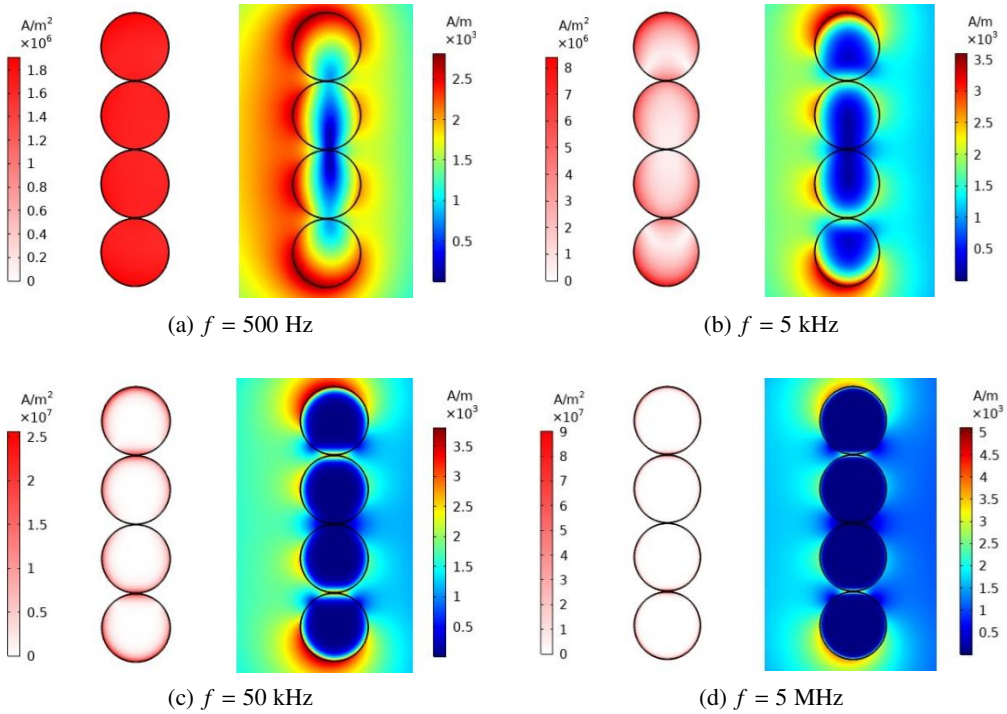


(a) $f$ = 500 Hz (b) $f$ = 5 kHz

(c) $f$ = 50 kHz (d) $f$ = 5 MHz

Fig. 6. The current density distribution across the conductors of a unit (left column), and the magnetic field at different frequencies (right column)

The distribution of current on the surface of the conductors depends on the frequency; as the frequency increases, the current distribution becomes more non-uniform, which increases the electrical resistance of the unit. Hence, as is shown in Fig. 7, the equivalent resistance of a unit at 5 MHz (110 mΩ) is about 323 times greater than its value at 10 Hz (0.34 mΩ).

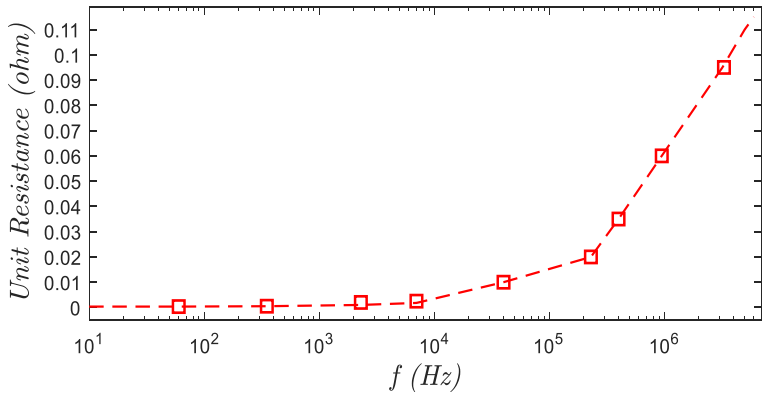


Fig. 7. The unit resistance curve in the studied frequency range

## 4. Verification of the simulation results

The simulated TFs of both test windings are presented in Fig. 8, and compared with each other. The inductive and capacitive elements of the models determine the resonance/anti-resonance frequencies, while the amplitudes of these points are affected by the resistance values [18]. Regarding the low frequency range, up to 100 kHz, the total equivalent inductances of both windings are the same. However, the subsequent resonant frequencies are different. Given that the model parameter values of both windings in Fig. 2 are identical, it can be concluded that the mentioned deviations in the TFs are caused by the different winding direction of the outer layers, as well as the electrical connection between the inner and outer layers in both windings. Since the first resonant frequency of the first test winding is lower than the second one, 328 kHz and 455 kHz, respectively, it can be concluded that the total equivalent capacitance of the first winding in the low frequency range is larger. Hence, it can be concluded that to achieve a desired resonant frequency, adjusting the winding direction of the inner and outer layers could be a cost-effective option.

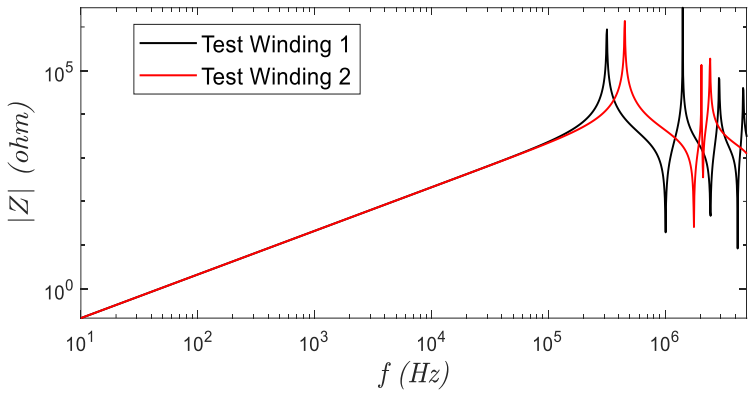


Fig. 8. The TF curves of the test windings computed by the simulations

The FRs of the windings are measured using a conventional FRA measuring test device, which is shown in Fig. 9. The sweep frequency measurement technique is used, in which 1601 frequency samples are swept by a logarithmic scale starting from 10 Hz and ending at 5 MHz. The equivalent circuit of the measurement, including the measuring device, is shown in Fig. 10. According to this figure, some internal 50 Ω resistors are used in the measuring device to suppress reflections in the measuring cables. The output of the FRA test device, $H(f)$, is as follows [19]:

$$H(f) = \frac{V_m(f)}{V_r(f)}, \tag{8}$$

where $V_r(f)$ and $V_m(f)$ are the reference (or input) and measured (or output) voltages of the test device respectively. Based on Fig. 10, the equivalent impedance of the test objects ($Z_{\mathrm{TO}}$) can be calculated as follows [19]:

$$Z_{\mathrm{TO}}(f) = \frac{V_{\mathrm{TO}}}{I_{\mathrm{TO}}} = \frac{V_r(f) - V_m(f)}{V_m(f)/50}. \tag{9}$$

Fig. 9. FRA measurement setup

In order to evaluate the accuracy of the simulated TF curves, they are compared with the measured results. In this regard, the simulation and measurement TFs of the first and second test windings are compared in Fig. 11 and Fig. 12, respectively. In both figures, in addition to the precise matching of the two TFs at low frequencies, the resonance/anti-resonance points in the HF range have reasonable accuracy. Likewise, the resonance/anti-resonance frequencies of the simulation and measurement TFs are presented in Table 3, which again confirms the accuracy of the simulation models.

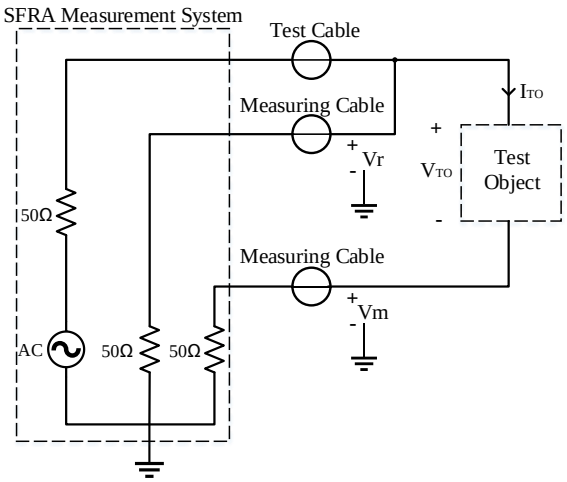


Fig. 10. The equivalent circuit of the FRA measurement

Table 3. The resonant points of the test windings estimated by the simulation and measurements

| | Resonance/ anti-resonance | Measurement (MHz) | Simulation (MHz) | Error (%) |
|---|---|---|---|---|
| **1st winding** | 1st | 0.343 | 0.328 | –4.37 |
| | 2nd | 0.889 | 0.921 | +3.59 |
| | 3rd | 1.25 | 1.34 | +7.20 |
| | 4th | 2.12 | 2.24 | +5.66 |
| **2nd winding** | 1st | 0.445 | 0.455 | +2.24 |
| | 2nd | 1.651 | 1.715 | +3.87 |
| | 3rd | 1.91 | 2.05 | +7.32 |
| | 4th | 2.55 | 2.445 | –4.11 |

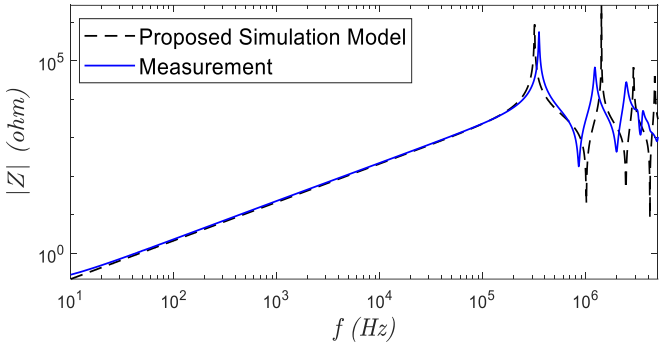


Fig. 11. The first test winding's response obtained by the simulation and measurement

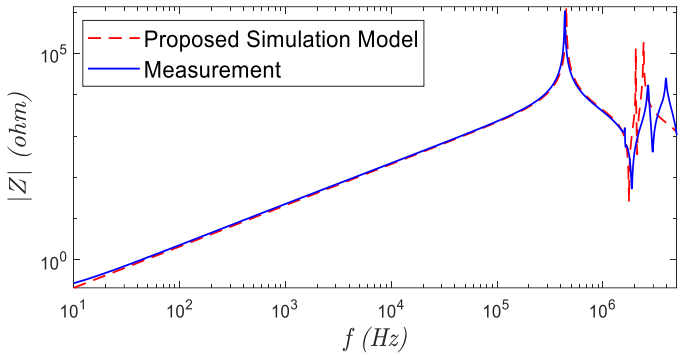


Fig. 12. The second test winding's response obtained by the simulation and measurement

## 5. Conclusion

This paper presents a simulation method for HF analysis of the solenoid windings by using a detailed model. To enhance the accuracy of the model and increase the valid upper frequency limit of the simulations to 5 MHz, the finite element method has been employed to obtain its parameters. In such a way, the effect of the electromagnetic phenomena occurring in the winding could be considered in estimating the precise values of the parameters. It was shown that the resistances and inductances of the model depend on the frequency.

Two different double-layer solenoids with various winding directions were constructed, and their detailed model equations were extracted. Then, the accuracy of the proposed method in HF ranges was validated by comparing the simulation and the measurement results. It was observed that the direction of the adjacent layers influences the resonance frequencies of the windings.

Relying on such a credible simulation method that provides an acceptable estimation of the frequency response of the windings, it will be possible to design and implement the HV filters with a desired resonant frequency.

### References

[1] Grandi G., Kazimierczuk M.K., Massarini A., Reggiani U., *Stray capacitances of single-layer Air-Core inductors for high frequency application*, IEEE, OH 45435, USA (1999), DOI: 10.1109/28.793378.

[2] Massarini A., Kazimierczuk M.K., Grandi G., *Lumped parameter models for single- and multiple-layer inductors*, PESC Record. 27th Annual IEEE Power Electronics Specialists Conference, Baveno, Italy, vol. 1, pp. 295–301 (1996), DOI: 10.1109/PESC.1996.548595.

[3] de Freitas Gutierres L.F., Cardoso G., *Analytical Technique for Evaluating Stray Capacitances in Multi-Conductor Systems: Single-Layer Air-Core Inductors*, IEEE Transactions on Power Electronics, vol. 33, no. 7, pp. 6147–6158 (2018), DOI: 10.1109/TPEL.2017.2745213.

[4] Massarini A., *Analytical Approach to the Calculation of Parasitic Capacitance Between Winding Turns*, 2018 IEEE 4th International Forum on Research and Technology for Society and Industry (RTSI), Palermo, Italy (2018), DOI: 10.1109/RTSI.2018.8548511.

[5] Rahimpour E., Christian J., Feser K., Mohseni H., *transfer function method to diagnose axial displacement and radial deformation of transformer windings*, IEEE Transactions on Power Delivery, vol. 18, no. 2, pp. 493–505 (2003), DOI: 10.1109/TPWRD.2003.809692.

[6] Lan Y., Yang L., Zhang X., Chen Q., Zheng Z., *Calculation Model of Parasitic Capacitance for High-Frequency Inductors and Transformers*, IEEE Access, vol. 11, pp. 143182–143189 (2023), DOI: 10.1109/ACCESS.2023.3341867.

[7] Liu X., Deng Z., Qiu Q., Wang R., Deng Y., He X., *Analytical Estimation Method of Winding Parasitic Capacitance for High-Frequency High-Voltage Application*, IEEE Access, vol. 8, pp. 73746–73755 (2020), DOI: 10.1109/ACCESS.2020.2987081.

[8] Shen Z., Wang H., Shen Y., Qin Z., Blaabjerg F., *An Improved Stray Capacitance Model for Inductors*, IEEE Transactions on Power Electronics, vol. 34, no. 11, pp. 11153–11170 (2019), DOI: 10.1109/TPEL.2019.2897787.

[9] Qin Yu, Holmes T.W., *A study on stray capacitance modeling of inductors by using the finite element method*, IEEE Transactions on Electromagnetic Compatibility, vol. 43, no. 1, pp. 88–93 (2001), DOI: 10.1109/15.917948.

[10] Popov M., van der Sluis L., Smeets R.P.P., *Complete analysis of Very Fast Transients in Layer-type Transformer Windings*, the International Conference on Power Systems Transients (IPST'07) in Lyon, France on June 4–7 (2007), DOI: 10.1109/TPWRD.2006.881605.

[11] Chagas N.B., Marchesan T.B., *Methodology for calculating the value of static capacitance between conductors of circular cross-section*, Brazilian Power Electronics Conference (COBEP), Juiz de Fora, Brazil, pp. 1–5 (2017), DOI: 10.1109/COBEP.2017.8257289.

[12] González-Teodoro J.R., Kindl V., Romero-Cadaval E., Asensi R., *Analysis of Skin Effect in Single Wire Resistance by Finite Element Methods*, IEEE 14th International Conference on Compatibility, Power Electronics and Power Engineering (CPE-POWERENG), Setubal, Portugal (2020), DOI: 10.1109/CPE-POWERENG48600.2020.9161540.

[13] Zhang H., Lee J.-H., Iyer N.M., Cao L., *New analytical equations for skin and proximity effects in interconnects operated at high frequency*, IEEE Electron Devices Technology and Manufacturing Conference (EDTM), Toyama, Japan (2017), DOI: 10.1109/EDTM.2017.7947499.

[14] Jiang L., Yan H., Meng J., Yin Z., Wei W., Wang Y., *Analysis of Eddy Current Effect and Loss Calculation of Transformer Winding Based on Finite Element Algorithm*, International Conference on Computer Systems, Electronics and Control (ICCSEC), Dalian, China (2017), DOI: 10.1109/ICCSEC.2017.8446892.

[15] Taghizadeh Kakhki M., Cros J., Viarouge P., *New Approach for Accurate Prediction of Eddy Current Losses in Laminated Material in the Presence of Skin Effect with 2-D FEA*, IEEE Transactions on Magnetics, vol. 52, no. 3, pp. 1–4 (2016), DOI: 10.1109/TMAG.2015.2481924.

[16] Rahimpour E., Tenbohlen S., *Fault diagnosis of actual large-power high-voltage windings using transfer function method*, Archives of Electrical Engineering, vol. 60, no. 3, pp. 269–281 (2011), DOI: 10.2478/v10171-011-0025-4.

[17] Bigdeli M., Vakilian M., Rahimpour E., *Comparison of transfer functions using estimated rational functions to detect winding mechanical faults in transformers*, Archives of Electrical Engineering, vol. 61, no. 1, pp. 85–99 (2012), DOI: 10.2478/V10171-012-0008-0.

[18] Gorecki K., Detka K., *Modeling of air transformers integrating ferrite plates for improved performance*, Archives of Electrical Engineering, vol. 73, no. 4, pp. 849–867 (2024), DOI: 10.24425/aee.2024.152099.

[19] Mirzaei H.R., *A Simple Fast and Accurate Simulation Method for Power Transformer Lightning Impulse Test*, IEEE Transactions on Power Delivery, vol. 34, no. 3, pp. 1151–1160 (2019), DOI: 10.1109/TPWRD.2019.2904864.